**PAPER**

# Numerical study of structural and magnetic properties of thin films obliquely deposited on rippled substrates

To cite this article: P N Solovev *et al* 2021 *J. Phys.: Condens. Matter* **33** 495802

View the article online for updates and enhancements.

# Numerical study of structural and magnetic properties of thin films obliquely deposited on rippled substrates

**P N Solovev[1],[*] , A V Izotov[1],[2] and B A Belyaev[1],[2]**

[1] Kirensky Institute of Physics, Federal Research Center KSC SB RAS, 50/38 Akademgorodok, 660036 Krasnoyarsk, Russia
[2] Siberian Federal University, 79 Svobodny pr., 660041 Krasnoyarsk, Russia

E-mail: psolovev@iph.krasn.ru

## Abstract

Structural modulation in thin films plays a substantial role in the formation of their magnetic properties. By producing topographic patterns in thin films, it is possible to engineer their magnetic response. Here, we report on the numerical study of the relationship between structural and static magnetic properties of thin films obliquely deposited on substrates with the sinusoidal surface. 3D Monte Carlo film growth simulations show that, under certain deposition conditions, an inhomogeneous columnar morphology can form in the films caused by the shadowing effect and the rippled substrate. Calculations of the demagnetizing tensors for these films demonstrate that their columnar structure is the source of the shape-induced uniaxial magnetic anisotropy that varies nonmonotonically with the deposition angle. Micromagnetic simulations of the generated films confirm the uniaxial character of the shape-induced anisotropy, and also show that magnetization reversal occurs via an incoherent rotation of magnetic moments.

Keywords: oblique deposition, micromagnetic simulation, thin film growth simulation, rippled substrate, magnetic anisotropy, magnetization reversal

(Some figures may appear in colour only in the online journal)

## 1. Introduction

In recent years thin magnetic films with artificially introduced structural modifications have gained increasing attention [1, 2]. The fabrication of such thin film nanostructures opens up new broad possibilities for controlling the magnetic properties of the samples to meet the specific needs of various applications, such as sensors, signal processing devices, and others. It has already been demonstrated that by creating a nonuniform periodic morphology in the films in a controllable way, it is possible to tailor their magnetic anisotropy [3–7], high-frequency response [8–10], and even magnetic relaxation [11].

Moreover, two decades ago, an exciting new research field of magnonics has emerged, which considers the propagation of magnons (the quanta of spin waves) in the magnets with properties periodically varied in space, known as magnonic crystals [12–14]. It is envisioned that the next generation data processing devices can be created on the basis of magnonic crystals.

A variety of methods have been suggested and successfully used to prepare nanopatterned magnetic structures. Lately, ion beam erosion processes have become widely used for the modification of substrate topography [1, 6, 7, 9, 15–20]. For certain irradiation conditions, such as ion incidence angle and ion energy, a nanoripple pattern can be created on the substrate, which on a local scale can be approximated by a sinusoidal surface, with the typical wavelengths of 20–400 nm and

[*] Author to whom any correspondence should be addressed.

amplitudes of 1.5–60 nm [6, 9]. Thin magnetic films grown on such substrates partially replicate their pattern, which results in the modification of the films' magnetic properties, most notably, their magnetic anisotropy [7]. Moreover, if magnetic material is deposited obliquely on a rippled substrate, inclined nanocolumnar structures can form on 'windward' slopes of the ripple due to the shadowing effect [17, 20]. This results in a more complex magnetic behavior of the samples but, on the other hand, expands our ability to adjust the properties of the films.

However, because the deposition process is of a random nature, the prediction of the microstructure of the resulting films and its influence on the magnetic characteristics is still a challenging problem. Three-dimensional Monte Carlo simulation is a very attractive method for solving this problem as this method models to some degree the real deposition process, thus allowing to study theoretically the growth dynamics of columnar structure developed in obliquely deposited films [21–23]. Numerical simulations of thin film growth and calculations of these film's magnetic responses can greatly contribute to our understanding of the microstructure and its connection to the magnetic properties of films as a function of deposition conditions. In this work, we explore numerically the structural and static magnetic properties of thin magnetic films obtained by the simulation of oblique deposition of particles on rippled substrates.

## 2. Methods

### 2.1. Film growth simulation

In this work, to investigate the relationship between structural and magnetic properties of the films obliquely deposited onto rippled substrates, we use our developed thin film growth simulator [24, 25]. The simulator makes it possible to generate three-dimensional structures with complex nanocolumnar morphology that closely resembles that of real obliquely deposited samples, given that the simulator's parameters were chosen appropriately. The simulator is based on a ballistic deposition model where a Monte Carlo approach is used to model the diffusion-limited aggregation process [26, 27]. Figure 1(a) shows a schematic picture of the deposition process. A discrete lattice configuration consisting of cubic cells is used. Each cell can be occupied by a cubic particle (growth unit) of size $\Delta$. A thin film is considered as an aggregate of these cubic particles.

At the first step of the growth simulation, a substrate is generated. As a substrate we use a sinusoidal surface that mimics to some extent real nanorippled substrates produced by oblique ion irradiation [18]. A deposited particle is initiated at a random location in the *xy* plane just above the surface of the film. This particle is then launched in a straight line toward the substrate at an incidence angle of $\alpha$ with respect to the surface normal (the *z*-axis). The incoming particle descends until it sticks to the previously deposited particles or the substrate. After that, the particle can diffuse over a film surface. The diffusion algorithm is based on a simple random walk model [26]. The diffusing particle jumps from one site to another (nearest
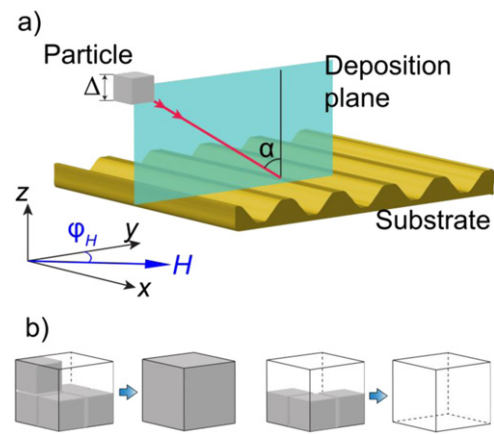


**Figure 1.** (a) Schematic view of an oblique deposition of a cubic particle at an incidence angle of $\alpha$ onto a rippled substrate, and the coordinate system, where $H$ is an in-plane magnetic field applied at an azimuthal angle of $\varphi_H$. (b) An illustration of a compression algorithm used for micromagnetic simulations.

vacancies) with a total number of the jumps $S$. The probability of the particle to diffuse from its current position $i$ to the nearest vacancy $j$ depends on the vacancy's number $N_j$ of the nearest neighbors (occupied cells), $P_{i \to j} = \exp(\gamma N_j) / \sum_j \exp(\gamma N_j)$. Here, $\gamma$ is a diffusion coefficient, and the summation is taken over all allowed vacancies. Periodic boundary conditions are implemented on all the vertical walls of the simulation. A more detailed explanation of the simulation procedure can be found in reference [24].

We simulated the oblique deposition of thin-film structures of size $256(x) \times 256(y) \times 120(z)\Delta^3$ onto the rippled substrate for various incidence angles $\alpha$, ranging from $0°$ to $80°$. Three sets of the diffusion parameters were used, resulting in the films of various densities: (i) $S = 1$, $\gamma = 1$ (low density films), (ii) $S = 5$, $\gamma = 0.44$ (intermediate density films), and (iii) $S = 8$, $\gamma = 0.8$ (high density films). The substrate was created by extruding a sinusoid along the *x*-axis, while the sinewave was directed along the *y*-axis (see figure 1(a)). The deposition plane (figure 1(a)) was oriented along the *y*-axis, that is, perpendicular to the substrate ripple. The parameters of the sinusoid were chosen to be typical of the averaged parameters measured for ion irradiated substrates: the wavelength was $\lambda = 50\Delta$, and the amplitude was $a = 10\Delta$. Comparing the simulated films with the real obliquely deposited films, we estimated the size of a particle to be $\Delta = 0.5$ nm [24]. Therefore, the wavelength of the ripple is $\lambda = 25$ nm, and its amplitude is $a = 5$ nm.

### 2.2. Calculation of shape-induced magnetic anisotropy

To determine the magnetic anisotropy of the simulated films induced by the dipolar interactions in nanocolumnar structure, we used a Fourier space approach introduced by Beleggia and De Graef [28]. With this approach, it is possible to calculate the demagnetizing tensor field for a magnetic sample of an arbitrary shape [29]. The problem of the magnetic vector potential calculation is simplified by a transition from real space to the Fourier space, where the calculation of the vector

potential transforms from a convolution operation to a vector product. The shape of the magnetic object can be described by its shape function $D(\mathbf{r})$ (where $\mathbf{r}$ is a radius vector in real space) [28], which equals unity in the regions of space occupied by the magnetic object and equals zero outside the object. The simulated films, which are three-dimensional arrays of zeroes (unoccupied cells) and ones (particles), are the discrete representations of the shape functions. As Beleggia and De Graef have shown, the volume averaged demagnetizing tensor of an object with the shape function $D(\mathbf{r})$ can be calculated using the following expression

$$N_{ij} = \frac{1}{8\pi^3 V} \int \mathrm{d}^3\mathbf{k} \frac{|D(\mathbf{k})|^2}{k^2} k_i k_j, \qquad (1)$$

where $V$ is the volume of a magnetic object, $D(\mathbf{k})$ is the Fourier transform of the shape function (shape amplitude), and $\mathbf{k}$ is the frequency vector. We made a fast Fourier transform of the 3D arrays representing the structure of the generated films, and then calculated numerically demagnetizing tensors $N_{ij}$ for each sample. The field $H_a$ of the magnetic uniaxial anisotropy originated from the dipolar interactions can be evaluated as

$$H_a = M_s(N_y - N_x), \qquad (2)$$

where $M_s$ is the saturation magnetization of the film, and $N_x$ and $N_y$ are the components of the diagonalized demagnetizing tensor $N_{ij}$. Note that if $H_a$ is positive, the magnetization easy axis (EA) lies along the $x$-axis otherwise, it is parallel to the $y$-axis.

### 2.3. Micromagnetic simulation

The magnetization reversal processes in the simulated thin-film structures were studied by using micromagnetic simulation [30, 31]. Each cell of the three-dimensional array occupied by a particle was characterized by a magnetic moment $M_i$ with the saturation magnetization $M_s$, while for unoccupied cells, $M_s = 0$. In the micromagnetic simulation, we considered energy terms for the exchange and dipolar interactions between discrete elements (particles) and the Zeeman energy term describing the interaction between magnetic moments $M_i$ and an in-plane applied magnetic field $H$. Note that we did not include explicitly any magnetic anisotropy energy terms in the micromagnetic model, thus only shape-induced magnetic anisotropy was presented in the investigated films. Periodic boundary conditions were applied to the exchange and dipolar interactions. The magnetic microstructure (equilibrium distribution of the magnetic moments $M_i$) of simulated films was determined from the solution of the system of linear inhomogeneous equations with undetermined Lagrange multipliers [30]. The magnetic parameters used in the simulations were typical of these for permalloy ($Ni_{80}Fe_{20}$): $M_s = 860$ emu cm$^{-3}$, and the exchange constant $1 \times 10^{-6}$ erg cm$^{-1}$. Note that the same value of $M_s$ was also used to calculate the shape-induced magnetic anisotropy using equation (2).

We applied a simple compression algorithm to the simulated films to reduce the computation time of the equilibrium magnetization distribution to a reasonable value (figure 1(b)).

The films were discretized on a cubic superlattice, each supercell of which consisted of eight cells of the original lattice. If more than half of the cells in the supercell were occupied, then the rest of the cells were populated by particles otherwise, all cells of the supercell were made unoccupied. For a special case when exactly half of the cells were occupied, the decision was made randomly. Then each supercell was merged. Thus, with this compression algorithm, we reduced the size of the films by eight times, to $128(x) \times 128(y) \times 60(z)\Delta^3$, while retaining the main features of their morphology. Note that the compressed films were used only in micromagnetic simulations.

## 3. Simulation results and discussion

### 3.1. Films structure

Figure 2 displays representative cross-section ($y$–$z$) images of the simulated films deposited on rippled substrates. These images were prepared in a way to be similar to the images of real samples obtained by transmission electron microscopy (TEM). For this, a slice in the $yz$ plane of thickness $\delta x$ was considered. For each ($y$, $z$) point in this slice, the local packing density $p_{yz}$ was calculated, determined as the number of occupied cells divided by the number of cells in thickness $\delta x$. This packing density distribution is represented as a two-dimensional normalized gray-scale map, where black corresponds to the maximum and white to the minimum local packing density.

Depending on the diffusion parameters (see subsection 2.1), three types of films were obtained: low density films, with the average packing density $p_0 = 0.33$ at the deposition angle of $\alpha = 0°$, intermediate density films with $p_0 = 0.81$ at $\alpha = 0°$, and high density films with $p_0 = 0.97$ at $\alpha = 0°$. The images in figure 2 indicate that at $\alpha = 0°$, the film of the lowest density has an almost amorphous morphology, and the sinewave substrate pattern practically does not present on the film surface. As the density of films increases from low to intermediate and high, a pronounced columnar structure starts to develop even at zero incidence angle. Note that the surface of the high density film retains the ripple structure of the substrate. At oblique incidence angles, inclined columns begin to grow on the substrate due to the shadowing mechanism [32]. The 'windward' slopes of substrate ripples act as seeds and depending on the deposition angle and diffusion parameters, columns formed on these seeds grow out through the whole film thickness or, due to the random nature of the deposition process, partly or completely lose the initial structure set by the substrate pattern. We note that these images of the simulated films look very similar to the TEM images captured for real metallic films obliquely deposited on rippled substrates (see, for example, reference [17]).

Figure 3 (top row) shows the top view of the fragments of the intermediate density films deposited at $\alpha = 0°$, $50°$, and $70°$. To investigate the microstructure of these films, we performed a two-dimensional fast Fourier transform (2D-FFT) analysis in the $xy$ plane for these films. 2D-FFT amplitude spectra calculated for an $xy$ layer at a height of $z = 30\Delta$
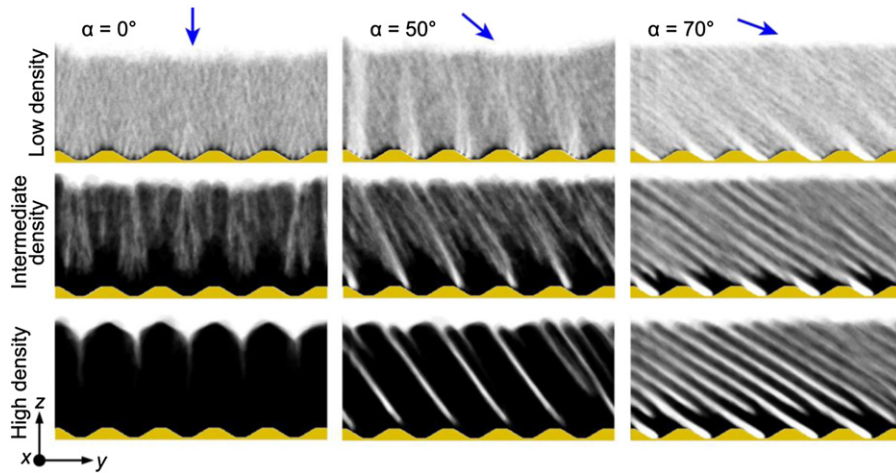
**Figure 2.** Cross-section ($y$–$z$) pseudo-TEM images of the structures (thin films) produced by the three-dimensional simulations of growth on rippled substrates. The films were deposited at various incidence angles $\alpha$ for three sets of the diffusion parameters resulting in low, intermediate, and high density films.
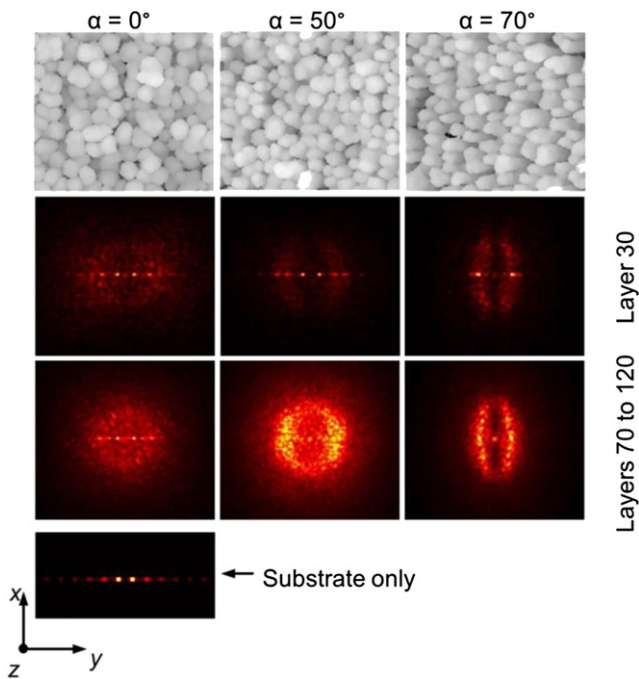


**Figure 3.** Top view of the intermediate density films simulated for incidence angles of $\alpha = 0°$, 50°, and 70° (top row; shown only fragments $170 \times 150\Delta^2$ of the whole $256 \times 256\Delta^2$ films). Below are 2D-FFT amplitude spectra, calculated for an $xy$ layer at a height of $z = 30\Delta$ (middle row), and obtained by averaging spectra of $xy$ layers from $z = 70$ to $120\Delta$ (bottom row). For reference, a spectrum of a pure substrate is also shown.



**Figure 4.** Dependences of the shape-induced anisotropy field $H_a$ on the deposition angle $\alpha$ for simulated films of various densities. Positive values of $H_a$ correspond to the direction of EA perpendicular to the deposition plane ($x$-axis) and negative to the direction of EA along the $y$-axis.

(figure 3, middle row) demonstrate some weak diffuse rings. But the maximum amplitude is observed at the same spatial frequency as that of the pure substrate, as can be easily seen from the comparison with the spectrum calculated just for the substrate (figure 3). This indicates that at a height not far away from the substrate, the morphology of the films is determined mostly by the ripple on the substrate for all the deposition angles.
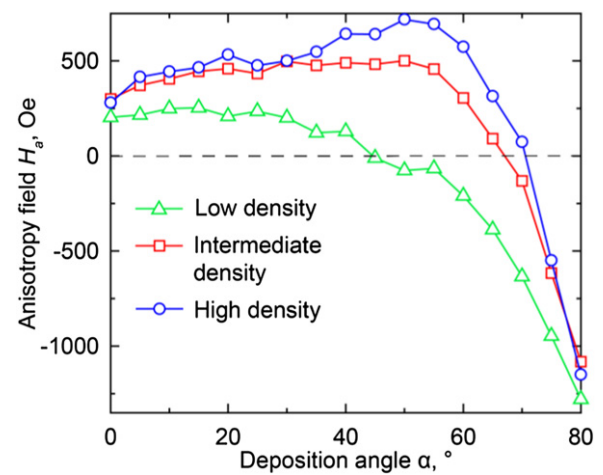
However, at larger heights, the FFT spectra change. The images obtained by averaging spectra of $xy$ layers from $z = 70$ to $120\Delta$ (figure 3, bottom row) show distinct rings, while the signal from the substrate is less evident. For the angle of $\alpha = 0°$, the ring is generally homogeneous, indicating the random distribution of columns over the substrate in the $xy$ plane, while the width of the ring corresponds to the degree of disorder in this distribution. As the deposition angle rises, the rings on the FFT spectra become increasingly inhomogeneous, showing that the columns are organized in a quasi-ordered way with a preferential direction oriented along the $x$-axis (parallel to the substrate ripple). However, the dominant wavelength of this quasi-periodic structure determined from the FFT spatial frequencies is significantly shorter than the substrate ripple wavelength $\lambda = 50\Delta$. For example, for $\alpha = 50°$, the dominant wavelength is $\approx 17\Delta$, and for $\alpha = 70°$ is $\approx 26\Delta$ ($\approx \lambda/2$), meaning that on each 'windward'
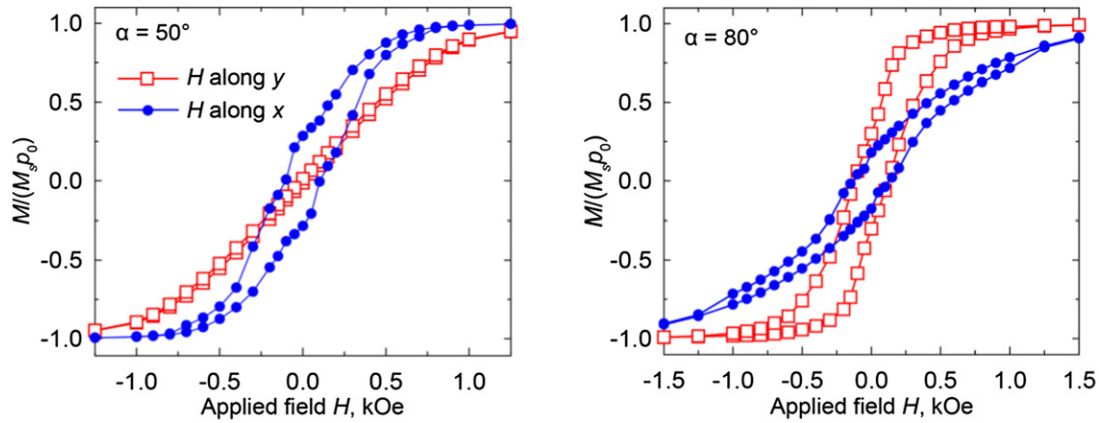
**Figure 5.** Magnetization reversal loops calculated by micromagnetic simulations of the intermediate density films deposited at angles of $\alpha = 50°$ and $80°$.

slope of ripple, several columns are grown along the *y*-axis, in accordance with figure 2. Apparently, this inhomogeneous morphology with a preferential direction should result in the occurrence of magnetic anisotropy of dipolar origin, i.e., the shape-induced magnetic anisotropy.

### 3.2. Magnetic properties

Using a Fourier space approach for the determination of demagnetizing tensors and equation (2), we have calculated the shape-induced uniaxial anisotropy field $H_a$ as a function of the deposition angle $\alpha$ for three types of simulated films of various densities (as discussed previously). Figure 4 shows the obtained results, where the positive values of $H_a$ correspond to the direction of EA along the *x*-axis (perpendicular to the deposition plane) and negative to the direction of EA along the *y*-axis. One can see that as the deposition angle increases, the magnetic anisotropy first increases as well until a maximum positive value, then abruptly decreases and, at some critical angle $\alpha_{cr}$, the EA even changes direction to 90°. Then the anisotropy increases again, reaching very large values of about 1.2 kOe. With the increase in films' density, the angle $\alpha_{cr}$ of the EA reorientation shifts toward higher values, and the maximum positive value of $H_a$ also increases. But for the lower and upper limits of the considered angular range, $\alpha = 0°$ and 80°, all three types of films have close values of the anisotropy field. It is important to note that the results presented in figure 4 are in good agreement with the experimental measurements of the magnetic anisotropy of obliquely deposited thin films [24, 32, 33].

The observed behavior of $H_a(\alpha)$ dependence is governed by the two processes occurring during film growth, columns aggregation and film's density decrease. Due to the shadowing effect and limited surface diffusion, the deposition of particles at incidence angles results in the growth of columns that tend to coalesce in the direction perpendicular to the deposition plane. Via the dipolar mechanism, this nonuniform morphology induces magnetic anisotropy, which EA is parallel to this direction. However, as the deposition angle increases, the porosity of the resulting films rises, and at a critical angle $\alpha_{cr}$, which depends on the diffusion parameters, the shape of

individual columns begins to play a key role. In this case, to minimize the dipolar energy, the magnetization must tilt toward the long axis of the columns, that is, EA is now directed along the deposition plane. Moreover, the substrate ripple enhances the shadowing effect leading to a more anisotropic growth of columns and, consequently, larger magnetic anisotropy fields.

The presence of ripples also results in the non-zero shape-induced anisotropy even for deposition at $\alpha = 0°$, in contrast to the case of a flat substrate [24]. For a thin solid film having sinusoidal corrugations on its both (top and bottom) surfaces, this anisotropy can be estimated using Schlomann expression [34] $H_a = 4\pi M_s \pi a^2 / \lambda d$, where $d$ is the film thickness. For the parameters of our films, this expression yields a value of 145 Oe that is somewhat smaller than the $H_a$ of the simulated at $\alpha = 0°$ films, which is about 250 Oe. This difference is related to the columnar structure of the simulated films, which partially (especially at the initial stages of growth) replicate the sinewave pattern on the substrate.

The above discussion on the origin of magnetic anisotropy in obliquely deposited films is also supported by the results of micromagnetic simulations. Figure 5 demonstrates hysteresis loops obtained with micromagnetic simulations of the intermediate density films deposited at angles of $\alpha = 50°$ and $80°$. The in-plane magnetic field $H$ was applied along the *y*-axis (square symbols) and *x*-axis (circles). Note that for ease of comparison, the loops were reduced to the product of the saturation magnetization and packing density, $M_s p_0$. For $\alpha = 50°$, the magnetization reversal curve along the *y*-axis shows practically no hysteresis, which is characteristic for magnetization reversal processes along the hard axis of the uniformly magnetized uniaxial ferromagnets. While the loop obtained for $H$ applied parallel to the *x*-axis exhibits quite large coercivity $H_c = 105$ Oe although it is about five times smaller than the anisotropy field calculated earlier for this film (figure 4). The shape of loops changes significantly for the film generated at a larger incidence angle of $\alpha = 80°$, with almost the same coercivity for both directions of the applied field.

The uniaxial character of the shape-induced magnetic anisotropy was confirmed by the angular dependence of the
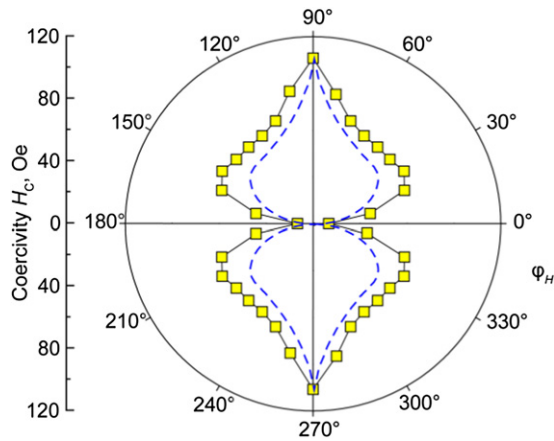
**Figure 6.** Polar plot of coercivity $H_c$ versus direction $\varphi_H$ of the in-plane applied field $H$. Symbols are the micromagnetic simulation results for the intermediate density film deposited at $\alpha = 50°$, and the dashed line is the results obtained from the Stoner–Wohlfarth model of a thin film with the uniaxial anisotropy field of 105 Oe.
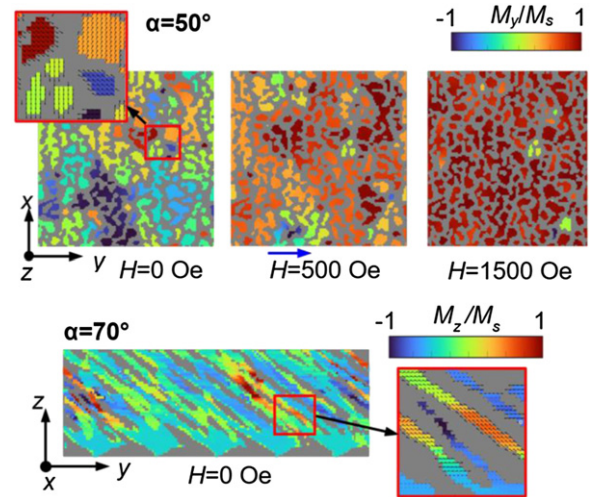


**Figure 7.** The equilibrium magnetization distributions obtained with micromagnetic simulations of the intermediate density films deposited at incidence angles of $\alpha = 50°$ and $70°$.

coercivity $H_c$ (figure 6), which was obtained from the hysteresis loops calculated for the intermediate density film deposited at $\alpha = 50°$, for various directions $\varphi_H$ of the applied field $H$. For reference, we also plotted in this figure the $H_c(\varphi_H)$ dependence (dashed line) calculated using the Stoner–Wohlfarth model [35] of a single domain thin magnetic film with the uniaxial anisotropy field of 105 Oe.

However, the obtained with micromagnetic simulations loops differ substantially from those expected for an ideal single-domain film with uniaxial anisotropy, whose loop along the EA is a rectangle with $H_c = H_a$, and along the hard axis is just an inclined straight line. This difference is related to the inhomogeneous microstructure of the simulated films that leads to the formation of complex magnetic configurations. Figure 7 shows representative images of the equilibrium magnetization distributions obtained by micromagnetic simulations of the intermediate density films deposited at $\alpha = 50°$ and $70°$. For $\alpha = 50°$, the distribution in the $xy$ layer at $z = 56\Delta$ is displayed for various strengths of the field $H$ applied along the $y$-axis, where the color corresponds to the projection of the magnetization on the $y$-axis. The exchange interaction enforces uniform alignment of the magnetic moments in individual columns, but due to the dipolar interactions, at zero applied field, the distribution of the integral magnetization of individual columns is in disorder (figure 7, $\alpha = 50°$, $H = 0$). The magnetization reversal occurs through the process of an incoherent rotation of the magnetic moments in separate regions of the film toward the $y$-axis.

As discussed earlier, the oblique deposition at grazing incidence angles yields very porous films consisting of conglomerates of weakly connected tilted columns. From simple consideration, it follows that in this case, at zero field, it is preferable for magnetic moments in the nearby columns to have an opposite direction to ensure the closed magnetic flux configuration and minimize the magnetostatic energy associated with magnetic 'chargers' on the opposite surfaces of the

film. This is partially confirmed by the results of micromagnetic simulations for the film deposited at $\alpha = 70°$ (figure 7). In the figure, the distributions for several overlaid $yz$ layers for $H = 0$ are shown, with the color corresponding to the projection of the magnetization on the $z$-axis. As one can see, the magnetic moments in individual columns indeed tend to orient along the columns' elongation axis, yet the overall magnetic structure is quite complex, mostly due to the interconnections between columns.

## 4. Conclusion

In this paper, by combining three numerical methods—film growth simulation, demagnetizing tensors calculation, and micromagnetic simulation—we have studied in detail the relationship between structural and magnetic properties of thin obliquely deposited films grown on the rippled substrates. The results showed that due to the shadowing effect enhanced by the substrate ripple an intricate inhomogeneous morphology consisting of interconnected nanocolumns was formed in the films. This morphology is the source of the shape-induced uniaxial magnetic anisotropy caused by the dipolar mechanism. The character of the calculated dependence of the magnetic anisotropy field on the deposition angle is similar to the experimental data reported in the literature, while the specific behavior is governed by the substrate ripple and the diffusion parameters used in the growth simulation. Micromagnetic simulations of the generated films revealed that due to the competition between the exchange and dipolar interactions a complex magnetic structure developed in the films, and magnetization reversal occurred via an incoherent rotation of the magnetic moments. These findings demonstrate that computer modeling is a powerful tool since the data obtained from three-dimensional simulations allow us to explain and predict the characteristics of real films.

## Acknowledgment

## Data availability statement

The data that support the findings of this study are available upon reasonable request from the authors.

## ORCID iDs

P N Solovev ⓘ https://orcid.org/0000-0003-3545-7599

## References

[1] Fassbender J *et al* 2009 Introducing artificial length scales to tailor magnetic properties *New J. Phys.* **11** 125002
[2] Lau J W and Shaw J M 2011 Magnetic nanostructures for advanced technologies: fabrication, metrology and challenges *J. Phys. D: Appl. Phys.* **44** 303001
[3] Moroni R, Sekiba D, Buatier de Mongeot F, Gonella G, Boragno C, Mattera L and Valbusa U 2003 Uniaxial magnetic anisotropy in nanostructured Co/Cu(001): from surface ripples to nanowires *Phys. Rev. Lett.* **91** 167207
[4] Oster J, Kallmayer M, Wiehl L, Elmers H J, Adrian H, Porrati F and Huth M 2005 Crystallography, morphology, and magnetic properties of Fe nanostructures on faceted $\alpha$-Al$_2$O$_3$ m plane *J. Appl. Phys.* **97** 014303
[5] Bubendorff J L, Zabrocki S, Garreau G, Hajjar S, Jaafar R, Berling D, Mehdaoui A, Pirri C and Gewinner G 2006 Origin of the magnetic anisotropy in ferromagnetic layers deposited at oblique incidence *Europhys. Lett.* **75** 119–25
[6] Liedke M O *et al* 2013 Crossover in the surface anisotropy contributions of ferromagnetic films on rippled Si surfaces *Phys. Rev.* B **87** 024424
[7] Arranz M A, Colino J M and Palomares F J 2014 On the limits of uniaxial magnetic anisotropy tuning by a ripple surface pattern *J. Appl. Phys.* **115** 183906
[8] McMichael R D, Twisselmann D J, Bonevich J E, Chen A P, Egelhoff W F and Russek S E 2002 Ferromagnetic resonance mode interactions in periodically perturbed films *J. Appl. Phys.* **91** 8647
[9] Körner M, Lenz K, Gallardo R A, Fritzsche M, Mücklich A, Facsko S, Lindner J, Landeros P and Fassbender J 2013 Two-magnon scattering in permalloy thin films due to rippled substrates *Phys. Rev.* B **88** 054405
[10] Langer M *et al* 2019 Spin-wave modes in transition from a thin film to a full magnonic crystal *Phys. Rev.* B **99** 024426
[11] Barsukov I *et al* 2012 Tuning magnetic relaxation by oblique deposition *Phys. Rev.* B **85** 014420
[12] Kruglyak V V, Demokritov S O and Grundler D 2010 *J. Phys. D: Appl. Phys.* **43** 264001
[13] Chumak A V, Serga A A and Hillebrands B 2017 Magnonic crystals for data processing *J. Phys. D: Appl. Phys.* **50** 244001
[14] Zakeri K 2020 Magnonic crystals: towards terahertz frequencies *J. Phys.: Condens. Matter* **32** 363001
[15] Oates T W H, Keller A, Noda S and Facsko S 2008 Self-organized metallic nanoparticle and nanowire arrays from ion-sputtered silicon templates *Appl. Phys. Lett.* **93** 063106
[16] Sarathlal K V, Kumar D and Gupta A 2011 Growth study of Co thin film on nanorippled Si(100) substrate *Appl. Phys. Lett.* **98** 123111
[17] Keller A, Peverini L, Grenzer J, Kovacs G J, Mücklich A and Facsko S 2011 Polycrystalline Ni thin films on nanopatterned Si substrates: from highly conformal to nonconformal anisotropic growth *Phys. Rev.* B **84** 035423
[18] Körner M, Röder F, Lenz K, Fritzsche M, Lindner J, Lichte H and Fassbender J 2014 Quantitative imaging of the magnetic configuration of modulated nanostructures by electron holography *Small* **10** 5161–9
[19] Koyiloth Vayalil S, Koorikkat A, Gopi A K, Roth S V and Anil Kumar P S 2020 Tailoring of uniaxial magnetic anisotropy in permalloy thin films using nanorippled Si substrates *J. Phys.: Condens. Matter* **32** 185804
[20] Bukharia K, Karmakar P, Pandit P and Gupta A 2021 Study of magnetic nanowires of amorphous Co$_{20}$Fe$_{60}$B$_{20}$ prepared by oblique angle deposition on nanorippled substrate *J. Magn. Magn. Mater.* **529** 167842
[21] Karabacak T 2011 Thin-film growth dynamics with shadowing and re-emission effects *J. Nanophotonics* **5** 052501
[22] Barranco A, Borras A, Gonzalez-Elipe A R and Palmero A 2016 Perspectives on oblique angle deposition of thin films: from fundamentals to devices *Prog. Mater. Sci.* **76** 59–153
[23] Bouaouina B, Mastail C, Besnard A, Mareus R, Nita F, Michel A and Abadias G 2018 Nanocolumnar TiN thin film growth by oblique angle sputter-deposition: experiments vs simulations *Mater. Des.* **160** 338–49
[24] Solovev P N, Izotov A V and Belyaev B A 2017 Microstructural and magnetic properties of thin obliquely deposited films: a simulation approach *J. Magn. Magn. Mater.* **429** 45–51
[25] Belyaev B A, Izotov A V and Solovev P N 2016 Growth simulation and structure analysis of obliquely deposited thin films *Russ. Phys. J.* **59** 301–7
[26] Suzuki M and Taga Y 2001 Numerical study of the effective surface area of obliquely deposited thin films *J. Appl. Phys.* **90** 5599–605
[27] Kaminska K, Suzuki M, Kimura K, Taga Y and Robbie K 2004 Simulating structure and optical response of vacuum evaporated porous rugate filters *J. Appl. Phys.* **95** 3055–62
[28] Beleggia M and De Graef M 2003 On the computation of the demagnetization tensor field for an arbitrary particle shape using a Fourier space approach *J. Magn. Magn. Mater.* **263** 1L–9
[29] Beleggia M, Graef M D and Millev Y T 2006 The equivalent ellipsoid of a magnetized body *J. Phys. D: Appl. Phys.* **39** 891–9
[30] Belyaev B A, Izotov A V and Leksikov A A 2010 Micromagnetic calculation of the equilibrium distribution of magnetic moments in thin films *Phys. Solid State* **52** 1664–72
[31] Izotov A V, Belyaev B A, Solovev P N and Boev N M 2021 Grain-size dependence of magnetic microstructure and high-frequency susceptibility of nanocrystalline thin films: a micromagnetic simulation study *J. Magn. Magn. Mater.* **529** 167856
[32] Smith D O, Cohen M S and Weiss G P 1960 Oblique-incidence anisotropy in evaporated permalloy films *J. Appl. Phys.* **31** 1755–62
[33] Kondorsky E and Denisov P 1970 On the origin of oblique-incidence anisotropy in evaporated cobalt films *IEEE Trans. Magn.* **6** 167–9
[34] Schlömann E 1970 Demagnetizing fields in thin magnetic films due to surface roughness *J. Appl. Phys.* **41** 1617–22
[35] Stoner E C and Wohlfarth E P 1948 A mechanism of magnetic hysteresis in heterogeneous alloys *Phil. Trans. R. Soc.* A **240** 599–642